

# Feature-EndoGaussian: Feature Distilled Gaussian Splatting in Surgical Deformable Scene Reconstruction

Kai Li<sup>\*1</sup> Junhao Wang<sup>\*1</sup> William Han<sup>2</sup> Ding Zhao<sup>2</sup>

<sup>1</sup>University of Toronto <sup>2</sup>Carnegie Mellon University

{kai.li, hry.wang}@mail.utoronto.ca

## Abstract

*Minimally invasive surgery (MIS) has transformed clinical practice by reducing recovery times, minimizing complications, and enhancing precision. Nonetheless, MIS inherently relies on indirect visualization and precise instrument control, posing unique challenges. Recent advances in artificial intelligence have enabled real-time surgical scene understanding through techniques such as image classification, object detection, and segmentation, with scene reconstruction emerging as a key element for enhanced intraoperative guidance. Although neural radiance fields (NeRFs) have been explored for this purpose, their substantial data requirements and slow rendering inhibit real-time performance. In contrast, 3D Gaussian Splatting (3DGS) offers a more efficient alternative, achieving state-of-the-art performance in dynamic surgical scene reconstruction. In this work, we introduce Feature-EndoGaussian (FEG), an extension of 3DGS that integrates 2D segmentation cues into 3D rendering to enable real-time semantic and scene reconstruction. By leveraging pretrained segmentation foundation models, FEG incorporates semantic feature distillation within the Gaussian deformation framework, thereby enhancing both reconstruction fidelity and segmentation accuracy. On the EndoNeRF dataset, FEG achieves superior performance (SSIM of 0.97, PSNR of 39.08, and LPIPS of 0.03) compared to leading methods. Additionally, on the EndoVis18 dataset, FEG demonstrates competitive class-wise segmentation metrics while balancing model size and real-time performance.*

## 1. Introduction

Surgical techniques have continuously evolved by addressing shortcomings in previous methods and observing their impact on patient recovery [26]. Traditionally, open surgery has been associated with extended healing periods, increased risk of infection, and permanent scarring. In contrast, mini-

mally invasive surgery (MIS), which gained popularity in the 1990s, offers reduced tissue damage, fewer post-operative complications, quicker recovery times, and shorter hospital stays [34]. MIS employs smaller incisions and utilizes an endoscope with an integrated camera to visualize internal organs, thereby generating surgical images and video data that can be further modeled and analyzed [1]. Although more than 80% of surgical procedures have transitioned to MIS [34], its success depends on high levels of technical skill and precision. Surgeons must operate while viewing an external monitor displaying the endoscopic feed, demanding exceptional hand-eye coordination and precise instrument control to avoid damage to adjacent tissues. This reliance on surgeon expertise underscores the need for assistive technologies that enhance patient safety and surgical performance.

Recent advancements in artificial intelligence (AI) and the decreasing cost of computational resources have enabled the development of automated methods to assist MIS in real time [1]. Tasks such as image classification [33], object detection [41], semantic segmentation [48], tissue tracking [35], and surgical scene reconstruction [42] have achieved state-of-the-art performance, significantly benefiting robotic-assisted MIS.

Surgical scene reconstruction has recently attracted considerable attention [18–20, 42]. By rendering the target area in real time, this technique provides surgeons with a comprehensive view that enhances navigation and instrument control, and it holds promise for enabling robotic surgery automation. Early methods were dominated by traditional techniques such as simultaneous localization and mapping (SLAM) [8, 32, 44], but the field has since transitioned to neural network-based approaches [15, 20] and, more recently, to neural radiance fields (NeRFs) [25, 42]. However, NeRF-based methods require large volumes of data and suffer from slow rendering speeds, motivating the development of 3D Gaussian Splatting (3DGS) [10] as a more efficient alternative. Landmark studies such as EndoGaussian [19] and LGS [17] have successfully applied 3DGS to surgical scene reconstruction.

More recently, feature field distillation tech-

<sup>\*</sup>Equal contribution

niques—initially developed for the NeRF domain [13, 31, 43]—have been extended to 3DGS [46, 47] beyond their application in surgical scene reconstruction. Inspired by these advances, we extend the 3DGS framework to support real-time segmentation and rendering by leveraging 2D segmentation foundation models [30, 48]. Our approach augments the traditional Gaussian deformation decoder with a lightweight MLP to predict per-Gaussian semantic feature updates and employs a CNN-based semantic decoder to align the rendered semantic feature map with features extracted by 2D segmentation models. This dual-level integration enables real-time, accurate semantic segmentation alongside high-fidelity scene reconstruction, effectively capturing dynamic tissue deformations and occlusions in MIS while identifying critical intraoperative objects.

In summary, our contributions are as follows:

1. We introduce Feature-EndoGaussian (FEG), a semantic extension of 3DGS for surgical scene reconstruction that integrates 2D segmentation cues directly into the 3D rendering process.
2. Despite the additional complexity introduced by semantic feature distillation, our approach enhances surgical scene understanding by producing high-quality segmentations comparable to standalone 2D models while simultaneously improving reconstruction fidelity and maintaining model size and FPS.

## 2. Related Work

### 2.1. Surgical Scene Reconstruction

Reconstructing soft tissues in robotic surgery from endoscopic stereo videos has been extensively studied, given its critical role in intraoperative navigation and automation of robotic-assisted procedures [18, 21, 28]. Traditional approaches predominantly rely on Simultaneous Localization and Mapping (SLAM) techniques [8, 9, 32, 44], though these methods often struggle in complex surgical environments due to dynamic, non-rigid tissue deformations, specular reflections, and occlusions introduced by surgical instruments. More recently, learning-based methods leveraging convolutional neural networks (CNNs) and vision transformers have improved stereo depth estimation and the modeling of non-rigid deformations [15, 20]. However, these approaches still face limitations when generalizing to highly dynamic and unstructured surgical scenes, particularly in conditions with poor depth cues and significant occlusions.

**Neural Radiance Fields** Neural radiance fields (NeRFs) [25] have emerged as a powerful framework for modeling 3D scenes with complex deformations. NeRF and its extensions have demonstrated impressive results in representing dynamic and deformable objects in non-surgical contexts [23, 27]. To address surgical-specific challenges, Wang et al.

[36] introduced EndoNeRF, a neural rendering algorithm optimized for 3D reconstruction in robotic surgery. By integrating dynamic NeRFs with surgical-specific refinements, EndoNeRF achieved state-of-the-art performance in both 3D reconstruction and deformation tracking. Nonetheless, NeRF-based methods [40] require querying radiance fields at numerous points and along many rays per image, resulting in significant computational overhead that impedes real-time performance [6, 29].

**Gaussian Splatting** To overcome the efficiency limitations of NeRF-based approaches, 3D Gaussian Splatting (3DGS) [10] has emerged as a fast and data-efficient alternative. By modeling scenes as anisotropic 3D Gaussians and employing tile-based rasterization, 3DGS facilitates real-time rendering while maintaining high-quality reconstruction. Several works have subsequently adopted 3DGS as the backbone for surgical scene reconstruction [7, 19, 39].

### 2.2. Surgical Scene Segmentation

In addition to real-time scene reconstruction, simultaneous segmentation of key anatomical structures and surgical instruments during intraoperative procedures is highly advantageous. Previous works have explored segmentation in endoscopic surgeries [5, 14, 37]. With recent advances in large-scale foundation models for segmentation, such as SAM [12] and SAM 2 [30], along with their adaptations to the medical domain (e.g., MedSAM [22], MedSAM 2 [48]), many approaches have fine-tuned these models for surgical applications. A recent study, Feature 3DGS [46], extends 3DGS to incorporate feature field distillation, enabling real-time segmentation, language-guided editing, and other interactive operations. Building on these developments, our work integrates 3DGS with feature field distillation to facilitate real-time rendering and segmentation of surgical scenes, thereby advancing intraoperative visualization.

## 3. Our Method

We propose FEG, an approach that extends the 3D Gaussian scene representation of EndoGaussian [19] and Feature3DGS [46] by incorporating semantic information from a 2D segmentation foundation model (e.g., SAM [12], SAM2 [30], and MedSAM [22]). From now on, we denote any 2D segmentation foundation model as SAM for simplicity, but we note that any segmentation model can be used. Our method integrates semantic cues at two levels. First, the standard Gaussian deformation decoder is augmented with an additional lightweight MLP, denoted  $F_{\text{feat}}$ , which predicts per-Gaussian semantic feature updates. Second, a separate CNN-based decoder processes the rendered semantic feature map to upsample and align it with the SAM-extracted features. A per-pixel  $L_1$  loss is imposed to ensure consistency

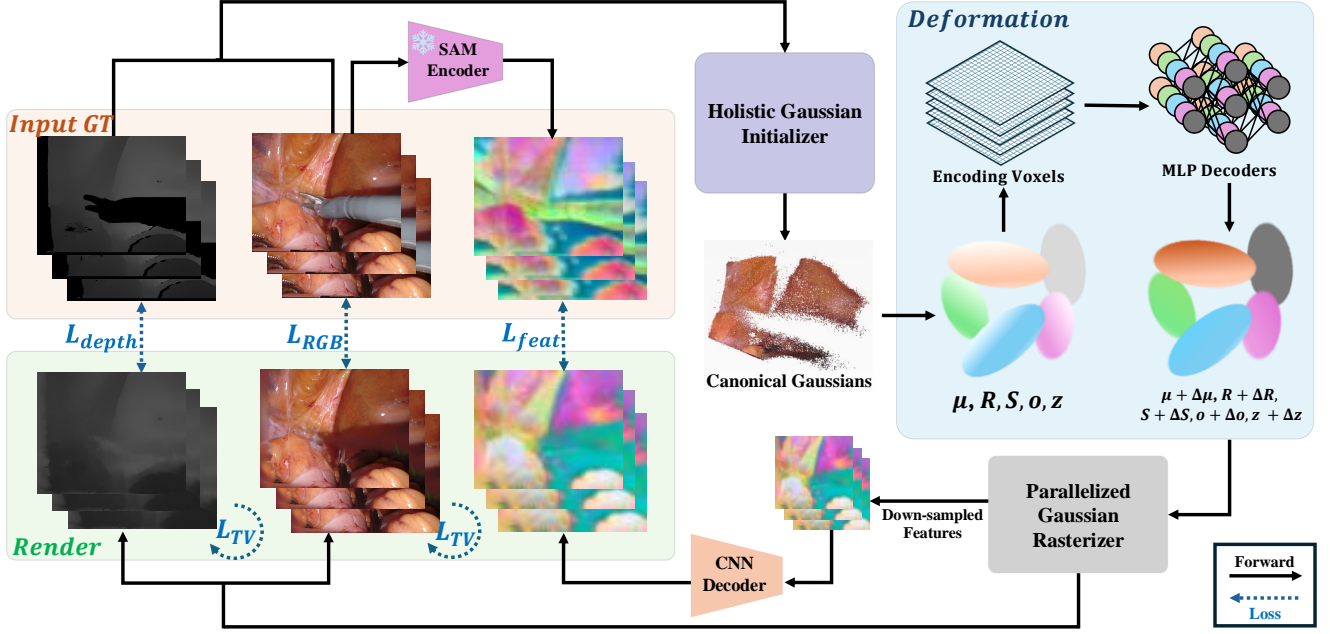


Figure 1. **Overview of FEG.** The process begins with holistic Gaussian initialization, where 3D Gaussians are re-projected from image pixels to form the initial scene representation. A 4D voxel encoder extracts latent features, which are then processed by a deformation decoder that predicts updates to the Gaussian parameters (position, rotation, scale, opacity) and incorporates semantic feature adjustments via a lightweight MLP. The updated Gaussians are rendered through a differentiable rasterizer to produce both radiance and semantic feature maps. Finally, a CNN-based decoder upsamples and aligns the rendered semantic features with those extracted from a 2D segmentation model (SAM), ensuring accurate semantic consistency across the scene.

between the rendered semantic features and those from the segmentation foundation model. We visualize a high level overview of our pipeline in Figure 1.

We introduce an updated rasterizer with parallelized implementation capable of simultaneously rendering color, depth, and the newly integrated semantic feature maps, enabling a more comprehensive representation for surgical scenes. Additionally, the rasterizer propagates depth-aware gradients explicitly to guide geometry refinement. Gradients for Gaussian mean and covariance terms are enhanced for improved shape accuracy. Alpha blending is adjusted for smoother handling of transparency gradients. Memory usage is optimized through cooperative groups for efficient execution. Further details are provided in the supplementary material.

### 3.1. 3D Gaussian Scene Representation and Initialization

Our method builds upon the 3D Gaussian Splatting (3DGS) framework [10], which represents a scene using a dense collection of 3D Gaussians. Each Gaussian is centered at a mean  $\mu$  and characterized by a covariance matrix  $\Sigma$  that defines its spatial spread. Specifically, the contribution of a

Gaussian at a 3D point  $\mathbf{x}$  is given by

$$G(\mathbf{x}) = \exp\left(-\frac{1}{2}(\mathbf{x} - \mu)^\top \Sigma^{-1}(\mathbf{x} - \mu)\right). \quad (1)$$

For both efficiency and interpretability, the covariance matrix is factorized as

$$\Sigma = R S S^\top R^\top, \quad (2)$$

where  $R$  is a rotation matrix and  $S$  is a scaling matrix. In this representation, the scene is modeled by jointly optimizing the parameters of each Gaussian—its position  $\mu$ , rotation  $R$ , scaling  $S$ , opacity  $o$ , and spherical harmonic (SH) coefficients.

Following Liu et al. [19], a holistic initialization is performed by re-projecting pixels from the input image sequence using estimated depth maps. For an image  $I_i$  with depth  $D_i$  and binary mask  $M_i$ , the corresponding 3D points are computed as

$$P_i = K^{-1} T_i D_i (I_i \odot M_i), \quad P = \bigcup_{i=1}^T P_i, \quad (3)$$

where  $K$  and  $T_i$  denote the camera intrinsic and extrinsic parameters, respectively.

### 3.2. Deformation Decoder with Semantic Feature Integration

To capture spatio-temporal deformations, each Gaussian is first encoded by a 4D voxel module that maps its center  $\mu$  and time  $t$  to a latent feature  $f$ . We follow EndoGaussian [19], where the authors were inspired by Wu et al. [38], Yang et al. [40] to represent the 4D voxel module as a multi-resolution HexPlane introduced by Cao and Johnson [4]. We also initialize a deformation decoder  $F$  consisting of four lightweight MLPs that predict deformations for position, rotation, scaling, and opacity:

$$\begin{aligned}\Delta\mu &= F_\mu(f), & \Delta R &= F_R(f), \\ \Delta S &= F_S(f), & \Delta o &= F_o(f),\end{aligned}\quad (4)$$

yielding the deformed Gaussian parameters

$$G_t = (\mu + \Delta\mu, R + \Delta R, S + \Delta S, o + \Delta o). \quad (5)$$

**MLP-Based Semantic Update:** In our approach, the deformation decoder is further extended with an additional MLP  $F_{\text{feat}}$  that predicts a semantic deformation:

$$\Delta z = F_{\text{feat}}(f). \quad (6)$$

Thus, each Gaussian’s latent semantic feature is updated as

$$z' = z + \Delta z, \quad (7)$$

resulting in an augmented Gaussian representation

$$G_t = (\mu + \Delta\mu, R + \Delta R, S + \Delta S, o + \Delta o, z'). \quad (8)$$

This mechanism allows the model to capture fine-grained semantic variations directly in the Gaussian parameter space.

**Semantic Feature Extraction:** For all experiments, we leverage a pretrained Segment Anything Model (SAM) [12] with a ViT-H encoder to extract semantic feature maps. Given an input image, SAM produces a high-dimensional semantic feature map at a spatial resolution of  $64 \times 64$  with 256 channels. To match the aspect ratio of the input images, we adopt the cropping procedure from [46]: an input image of size  $H \times W$  (with  $W > H$ ) yields a cropped feature map of size  $64 \times \frac{64W}{H}$ , preserving semantic information without introducing padding artifacts. The resulting feature maps serve as supervision signals during training. To improve computational efficiency without sacrificing semantic expressivity, we compress the rendered feature maps to 128 dimensions, which is updated through the semantic MLP branch  $F_{\text{feat}}$  as defined in Equation (6).

### 3.3. Differentiable Rendering and Loss Functions

During rendering, both the radiance (color) and semantic feature fields are computed via front-to-back alpha blending.

For a pixel  $\mathbf{x}$ , the rendered color  $\hat{C}(\mathbf{x})$  and semantic feature  $\hat{z}(\mathbf{x})$  are given by

$$\hat{C}(\mathbf{x}) = \sum_{i=1}^N c_i \alpha_i \prod_{j=1}^{i-1} (1 - \alpha_j), \quad (9)$$

$$\hat{z}(\mathbf{x}) = \sum_{i=1}^N z'_i \alpha_i \prod_{j=1}^{i-1} (1 - \alpha_j), \quad (10)$$

where  $c_i$  and  $z'_i$  denote the color and updated semantic feature contributions from the  $i$ th Gaussian, and  $\alpha_i$  is its effective opacity. The effective opacity is computed by evaluating a corresponding 2D covariance matrix:

$$\Sigma'_i = J W \Sigma_i W^\top J^\top, \quad (11)$$

with  $J$  representing the Jacobian of the affine approximation of the projective transformation and  $W$  the view transformation matrix.

**CNN-Based Semantic Decoder:** After differentiable rasterization, a CNN-based decoder is employed to upsample the rendered semantic feature map so that its channel dimension match those of the SAM-extracted features. This decoder performs a simple pointwise convolution aligning the feature dimensionality to match SAM’s output. The resulting semantic feature map is then compared, using a per-pixel  $L_1$  loss, to the high-level semantic features  $f_{\text{SAM}}$ :

$$\mathcal{L}_{\text{feat}} = \frac{1}{HW} \sum_{\mathbf{x} \in \Omega} \|\hat{z}(\mathbf{x}) - z_{\text{SAM}}(\mathbf{x})\|_1, \quad (12)$$

where  $\Omega$  denotes the set of pixel coordinates in an image of resolution  $H \times W$ .

In addition to the photometric loss  $\mathcal{L}_{\text{rgb}}$  and depth loss  $\mathcal{L}_{\text{depth}}$  (as in [19]), the overall loss is defined as

$$\mathcal{L} = \lambda_{\text{rgb}} \mathcal{L}_{\text{rgb}} + \lambda_{\text{depth}} \mathcal{L}_{\text{depth}} + \lambda_{\text{feat}} \mathcal{L}_{\text{feat}} + \lambda_{\text{TV}} \mathcal{L}_{\text{TV}}, \quad (13)$$

with  $\mathcal{L}_{\text{TV}}$  enforcing spatio-temporal smoothness [19]. The hyperparameter are fixed at  $\lambda_{\text{rgb}} = 1$ ,  $\lambda_{\text{depth}} = 0.01$ ,  $\lambda_{\text{feat}} = 1$ , and  $\lambda_{\text{TV}} = 0.03$ .

### 3.4. Training and Inference

The complete optimization is performed in a coarse-to-fine manner. In the coarse stage, only the basic Gaussian parameters are updated. In the fine stage, the semantic branch—comprising both the MLP  $F_{\text{feat}}$  within the deformation decoder and the CNN-based semantic decoder—is activated. This enables the network to jointly optimize the 3D Gaussian parameters and all MLP weights (including those of  $F_{\text{feat}}$ ) using the Adam optimizer, while the CNN-based decoder ensures that the rendered semantic feature map is accurately aligned with the SAM features.



Table 1. Baselines for surgical scene reconstruction on ENDONERF [36] and SCARED [3]

Dataset	Method	SSIM ( $\uparrow$ )	PSNR ( $\uparrow$ )	LPIPS ( $\downarrow$ )
ENDONERF [36]	EndoNeRF [36]	0.93	36.06	0.09
	EndoSurf [42]	0.95	36.53	0.07
	LerPlane-9k [40]	0.93	34.99	0.08
	LerPlane-32k [40]	0.95	37.38	0.05
	EndoGS [45]	0.96	37.29	0.05
	EndoGaussian [19]	0.96	37.78	0.05
	LGS [17]	0.96	37.48	0.07
	<b>FEG (Ours)</b>	<b>0.97</b>	<b>39.08</b>	<b>0.03</b>
SCARED [3]	EndoNeRF [36]	0.77	24.35	0.40
	EndoSurf [42]	0.80	25.02	0.36
	EndoGaussian [19]	0.83	26.89	0.27
	LGS [17]	<b>0.83</b>	27.05	0.30
	<b>FEG (Ours)</b>	0.77	<b>27.18</b>	<b>0.23</b>

During inference, segmentation masks are generated by decoding the rendered and upsampled semantic features using SAM’s pretrained decoder. To facilitate accurate multi-instance segmentation, class-specific bounding box prompts derived from ground truth annotations are provided as input. The inference process can be summarized as:

$$\hat{z}(\mathbf{x}) = \text{FEG}_{\text{render}}(G_t, \mathbf{x}), \quad (14)$$

$$\hat{z}'(\mathbf{x}) = \text{FEG}_{\text{decoder}}(\hat{z}(\mathbf{x})), \quad (15)$$

$$\hat{M}(\mathbf{x}) = \text{SAM}_{\text{decoder}}(\hat{z}'(\mathbf{x}), B), \quad (16)$$

where  $\hat{z}(\mathbf{x})$  represents the rendered semantic feature at pixel  $\mathbf{x}$ ,  $\hat{z}'(\mathbf{x})$  is the upsampled feature map,  $B$  denotes bounding box prompts, and  $\hat{M}(\mathbf{x})$  is the resulting segmentation mask.

We follow the experimental setup and configurations from EndoGaussian [19] for evaluation consistency, noting that further hyperparameter tuning on specific datasets, such as the EndoVis18 dataset [2], may yield additional performance improvements.

## 4. Experiments

### 4.1. Experimental Setup

We optimize both the original Gaussian features and the Hexplane deformations [4] using the Adam optimizer [11]. Following Liu et al. [19], we first optimize the canonical (coarse) gaussians for 1000 iterations and then train the full FEG model for an additional 6000 iterations. To ensure stable convergence, we apply an exponential learning rate decay schedule. All experiments are conducted on NVIDIA A5000 24GB GPUs. We provide a detailed breakdown of all hyperparameters used, including learning rates for different parameter groups, decay schedules, and other tuning adjustments in the supplementary material.

### 4.2. Datasets

For surgical scene reconstruction, we use the EndoNeRF [36] and SCARED [3] datasets. For segmentation tasks, we utilize the EndoVis18 [2] dataset.

Table 2. Class-wise multilabel segmentation results on the EndoVis18 dataset

Model	Class	IoU ( $\uparrow$ )	DSC ( $\uparrow$ )	Recall ( $\uparrow$ )	Precision ( $\uparrow$ )
FEG (ViT-H)	kidney	0.85	0.91	0.95	0.89
	small intestine	0.82	0.90	0.92	0.88
	instrument shaft	0.33	0.37	0.35	0.66
	instrument clasper	0.25	0.36	0.31	0.64
	clamps	0.27	0.39	0.32	0.68
	instrument wrist	0.68	0.80	0.89	0.75
SAM (ViT-H)	kidney	0.85	0.91	0.92	0.92
	small intestine	0.85	0.92	0.93	0.90
	instrument shaft	0.32	0.37	0.34	0.66
	instrument clasper	0.26	0.36	0.31	0.65
	clamps	0.28	0.40	0.32	0.69
	instrument wrist	0.76	0.85	0.87	0.85
SAM (ViT-B)	kidney	0.80	0.89	0.93	0.86
	small intestine	0.85	0.92	0.93	0.90
	instrument shaft	0.32	0.37	0.34	0.60
	instrument clasper	0.26	0.36	0.32	0.63
	clamps	0.28	0.40	0.32	0.69
	instrument wrist	0.76	0.85	0.86	0.85
MedSAM (ViT-B)	kidney	0.83	0.90	0.90	0.91
	small intestine	0.84	0.91	0.94	0.88
	instrument shaft	0.32	0.36	0.34	0.74
	instrument clasper	0.25	0.35	0.30	0.74
	clamps	0.24	0.36	0.28	0.73
	instrument wrist	0.71	0.81	0.79	0.89
SAM 2 (Hiera-T)	kidney	0.85	0.92	0.90	0.94
	small intestine	0.83	0.88	0.87	0.91
	instrument shaft	0.84	0.90	0.93	0.90
	instrument clasper	0.36	0.48	0.59	0.58
	instrument wrist	0.40	0.46	0.49	0.45
	clamps	0.66	0.79	0.88	0.72
SAM 2 (Hiera-H)	kidney	0.87	0.93	0.92	0.94
	small intestine	0.90	0.94	0.95	0.94
	instrument shaft	0.83	0.90	0.92	0.90
	instrument clasper	0.69	0.67	0.84	0.69
	instrument wrist	0.38	0.45	0.50	0.43
	clamps	0.66	0.79	0.87	0.72

We utilize the cutting and pulling sets from EndoNeRF, which consist of two in-vivo prostatectomy cases captured with stereo cameras from a single viewpoint. The pulling and cutting sets contain 63 and 156 frames, respectively. Following previous works [42], we select every eighth frame for testing.

The SCARED dataset comprises RGB-D scans of porcine cadaver abdominal anatomy and includes seven sequences. In line with protocols from EndoGaussian [19] and LGS, we use a subset of five sequences—datasets 1, 2, 3, 6, and 7. For each selected sequence, we render the first keyframe and use all frames within that keyframe, denoted as d1k1 (197 frames), d2k1 (88 frames), d3k1 (329 frames), d6k1 (637 frames), and d7k1 (647 frames). A 7:1 train-test split is adopted, consistent with prior works [19].

For segmentation evaluation, we employ the EndoVis18 dataset [2], which consists of four sets of 149 frames capturing diverse surgical scenes. Sets 2, 3, and 4 are used for training, while set 1 is reserved for testing—with a 60-frame video from set 1 evaluating our integrated rendering and segmentation pipeline. Note that the dataset is designed for segmentation rather than surgical scene reconstruction and thus lacks per-frame camera calibrations and poses. In addition, motion blur and low frame rates further increase the

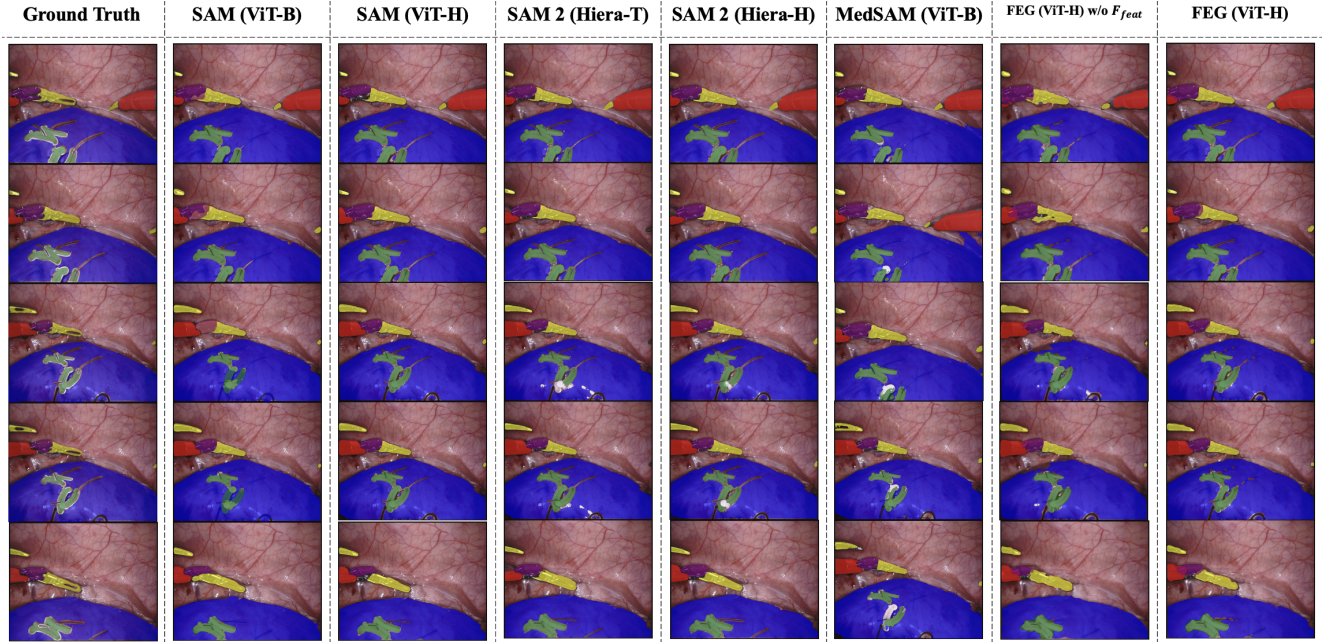


Figure 2. Qualitative segmentation comparisons. From left to right: our full FEG model, FEG without the 5th MLP, MedSAM (ViT-B), SAM 2 (Hiera-H), SAM 2 (Hiera-T), SAM (ViT-H), SAM (ViT-B), and the ground truth segmentation mask. Colors correspond to the following classes: kidney (blue), small intestine (orange), instrument shaft (red), instrument clasper (yellow), instrument wrist (purple), and clamps (green).

Table 3. Comparison of model size in megabytes (MB) and frames per second (FPS) between EndoGaussian [19] and FEG

Method	Size MB ( $\downarrow$ )	FPS ( $\uparrow$ )
EndoGaussian [19]	334.50	22.50
<b>FEG (Ours)</b>	392.50	13.32

difficulty of high-quality reconstruction. Consequently, we report metrics computed between the ground truth semantic segmentation masks and the decoded semantic features rendered by FEG during training, and compare these results with the zero-shot performance of 2D segmentation foundation models.

We consider two segmentation tasks: multilabel segmentation for six classes (kidney, small intestine, instrument shaft, instrument clasper, instrument wrist, clamps) and binary segmentation, where all foreground classes are merged.

### 4.3. Main Results

We now discuss the performance of FEG in both rendering and segmentation, comparing our method against existing approaches and evaluating various ablations.

**Rendering Results** Table 1 reports the quantitative results for surgical scene reconstruction. For the EndoNeRF dataset

Table 4. Comparison across different segmentation foundation models and two modes of FEG for binary segmentation on the EndoVis18 dataset [3]

Model	IoU ( $\uparrow$ )	DSC ( $\uparrow$ )	Recall ( $\uparrow$ )	Precision ( $\uparrow$ )
SAM (ViT-B)	0.85	0.92	0.95	0.89
SAM (ViT-H)	0.86	0.92	0.94	0.91
SAM 2 (Hiera-T)	0.82	0.90	0.89	0.91
SAM 2 (Hiera-H)	0.84	0.92	0.93	<b>0.93</b>
MedSAM (ViT-B)	0.84	0.91	0.92	0.91
<b>FEG (ViT-H) w/o <math>F_{feat}</math></b>	0.79	0.88	0.86	0.90
<b>FEG (ViT-H)</b>	<b>0.86</b>	<b>0.92</b>	<b>0.95</b>	0.90

[36], we average the performance over the pulling and cutting sets. FEG achieves superior performance across all metrics, even with the added complexity of simultaneously rendering semantic features. On the SCARED dataset [3], FEG attains the best PSNR and LPIPS scores while yielding comparable SSIM values. We conjecture that the incorporation of semantic features enhances geometric consistency during reconstruction. We provide rendering visualizations on the cutting and pulling sets on the EndoNeRF dataset [36] in Figure 3 and additional renderings on the EndoVis18 [2] dataset in the supplementary material.

**Rendering Speed** A key advantage of 3DGS methods [10] is the improved rendering speed relative to NeRF-based approaches [25]. Table 3 presents the model size (in MB) and



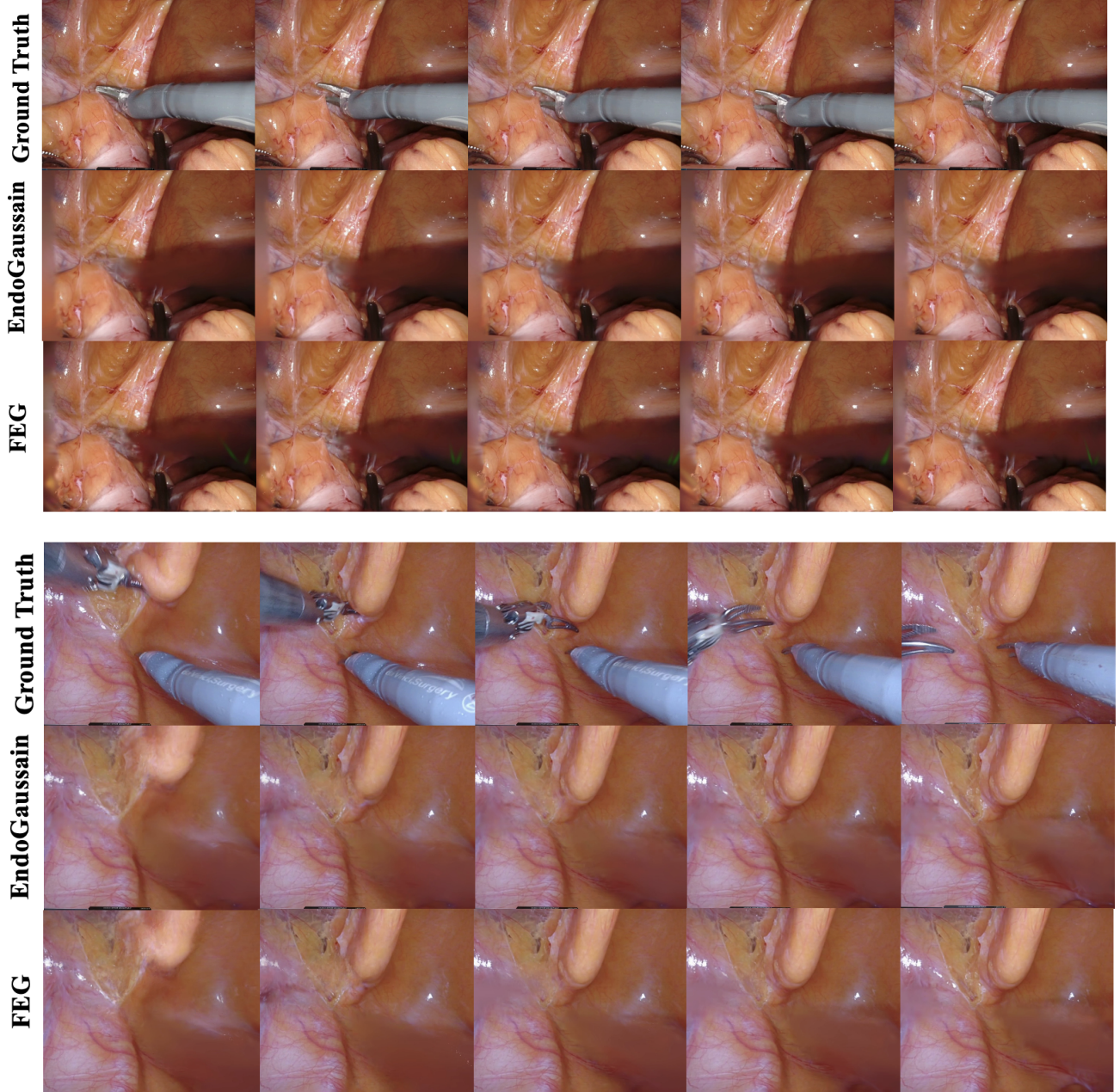


Figure 3. Comparison of qualitative renderings between EndoGaussian [19], FEG, and ground truth on the cutting (top) and pulling (bottom) sets of the EndoNeRF dataset [36]. We can see that across all scenes, FEG and EndoGaussian experience similar performances, although FEG is able to capture semantic features which can then later be used for segmentation.

frames per second (FPS) for FEG and EndoGaussian [19] on the A5000 GPU. Despite the additional complexity for semantic processing, FEG maintains competitive FPS and model size. Figure 3 shows qualitative renderings comparing EndoGaussian, FEG, and ground truth on the EndoNeRF Dataset. Both FEG and EndoGaussian demonstrate similar rendering quality, with FEG providing the added benefit of

semantic feature extraction for segmentation.

**Results on Segmentation** Tables 4 and 5 report the binary and multilabel segmentation performance on the EndoVis18 dataset [2]. For multilabel segmentation, Table 5 shows the averaged results, while Table 2 provides the detailed per-class performance. In the binary setting, FEG with  $F_{\text{feat}}$

Table 5. Weight-averaged scores for multilabel segmentation on the EndoVis18 dataset [3].

Model	IoU ( $\uparrow$ )	DSC ( $\uparrow$ )	Recall ( $\uparrow$ )	Precision ( $\uparrow$ )
SAM (ViT-B)	0.65	0.73	0.75	0.79
SAM (ViT-H)	0.68	0.75	0.74	0.84
SAM 2 (Hiera-T)	0.77	0.85	<b>0.88</b>	0.84
SAM 2 (Hiera-H)	<b>0.79</b>	<b>0.87</b>	0.87	<b>0.88</b>
MedSAM (ViT-B)	0.66	0.74	0.86	0.72
<b>FEG (ViT-H) w/o <math>F_{\text{feat}}</math></b>	0.63	0.73	0.72	0.82
<b>FEG (ViT-H)</b>	0.68	0.75	0.76	0.82

achieves the best IoU, DSC, and recall scores, while maintaining competitive precision compared to state-of-the-art models such as SAM 2 [30]. For multilabel segmentation, FEG is competitive with models like SAM (ViT-B/H) and MedSAM, though SAM 2 shows superior performance in some classes (e.g., clamps). This discrepancy suggests that while FEG captures high-level semantic features effectively, further refinement is needed to encode more class-specific details. It is important to note that unlike SAM, which focuses solely on 2D segmentation, FEG performs real-time rendering and segmentation simultaneously. This difference makes a direct comparison with SAM somewhat unfair, as there is currently no NeRF-equivalent or Gaussian Splitting model that integrates segmentation for endoscopic datasets. Despite this, FEG still delivers comparable performance in multilabel segmentation and even excels in binary segmentation compared to standalone SAM models. Qualitative results are provided in Figure 2, with additional visualizations available in the supplementary material.

#### 4.4. Ablation Study

**Component Analysis:** Table 6 presents an ablation study that highlights the contribution of each key component in FEG to the overall rendering quality. Removing the semantic MLP  $F_{\text{feat}}$  — responsible for updating per-Gaussian semantic features — results in a moderate performance drop. This indicates that while the basic geometric deformation is maintained, the absence of fine-grained semantic updates slightly hinders the model’s ability to capture detailed semantic variations. Similarly, omitting the per-pixel  $L_1$  feature loss significantly degrades the alignment between the rendered semantic features and those extracted from the segmentation foundation model (SAM), as reflected by the increased L1 error. This misalignment confirms the importance of explicit semantic supervision in guiding the CNN-based semantic decoder. Most notably, excluding the HexPlane component [4], which is integral to the 4D voxel module for capturing spatio-temporal deformations, leads to a drastic decline in reconstruction quality. This substantial drop underscores the critical role of the HexPlane in providing robust deformation representations that are essential for high-fidelity scene reconstruction.

Table 6. Ablation study on how removing different components of FEG alters rendering performances on the EndoNeRF dataset [36].

Model	SSIM ( $\uparrow$ )	PSNR ( $\uparrow$ )	LPIPS ( $\downarrow$ )	L1 Feature Loss ( $\downarrow$ )
w/o $F_{\text{feat}}$	0.97	38.56	0.04	0.10
w/o L1 Feature Loss	0.97	38.43	0.04	0.18
w/o HexPlane [4]	0.88	26.65	0.17	0.06
<b>FEG (Ours)</b>	<b>0.97</b>	<b>39.08</b>	<b>0.03</b>	<b>0.03</b>

Table 7. Ablation study on how finetuning SAM improves segmentation and rendering on the EndoVis18 dataset [3].

Finetuned	IoU ( $\uparrow$ )	DSC ( $\uparrow$ )	SSIM ( $\uparrow$ )	PSNR ( $\uparrow$ )
X	0.60	0.73	0.67	<b>20.43</b>
✓	<b>0.69</b>	<b>0.81</b>	<b>0.67</b>	20.37

**Finetuning SAM:** Table 7 compares segmentation and rendering performance using the original versus the finetuned SAM model (trained on EndoVis18 [2] sets 2, 3, and 4). Finetuning significantly improves segmentation metrics—IoU and DSC—demonstrating that adapting SAM to the domain-specific characteristics of endoscopic scenes yields more accurate semantic cues. These enhanced semantic features, in turn, facilitate better guidance during rendering, as reflected by comparable SSIM and PSNR scores. Overall, the results affirm that task-specific refinement of the segmentation backbone is important in boosting both segmentation fidelity and the subsequent rendering quality.

## 5. Conclusion

We introduced Feature EndoGaussian (FEG), an extension of EndoGaussian [19] inspired by Feature 3DGS [46], which enables simultaneous surgical scene reconstruction and multilabel semantic segmentation of dynamic endoscopic scenes. FEG integrates distilled feature fields from 2D segmentation foundation models directly into the 3D rendering process, and despite the additional complexity, it consistently improves reconstruction quality over existing baselines. In binary segmentation, FEG achieves state-of-the-art performance, and in the multilabel setting, it remains competitive against robust 2D segmentation models. Moreover, FEG maintains similar FPS and model size compared to its counterparts, preserving the key advantage of 3DGS methods in real-time applications.

This work has notable limitations, primarily due to the scarcity of high-quality endoscopic datasets that provide both reconstruction and segmentation data. For instance, while EndoVis18 [2] offers segmentation masks, the low image quality adversely affects rendering performance. We hope this work encourages the collection of multimodal data—incorporating distillable semantic features such as text, images, and audio—that can be seamlessly integrated into our pipeline. Additionally, our approach lays the ground-



work for future extensions beyond reconstruction and segmentation, such as language-guided editing and promptable segmentation, as suggested by related work in Feature 3DGS [46] and NeRF-DFF [13].

## References

- [1] Mansoor Ali, Rafael Martinez Garcia Pena, Gilberto Ochoa Ruiz, and Sharib Ali. A comprehensive survey on recent deep learning-based methods applied to surgical data, 2023. 1
- [2] Max Allan, Satoshi Kondo, Sebastian Bodenstedt, Stefan Leger, Rahim Kadkhodamohammadi, Imanol Luengo, Felix Fuentes, Evangello Flouty, Ahmed Mohammed, Marius Pedersen, Avinash Kori, Varghese Alex, Ganapathy Krishnamurthi, David Rauber, Robert Mendel, Christoph Palm, Sophia Bano, Guinther Saibro, Chi-Sheng Shih, Hsun-An Chiang, Juntang Zhuang, Junlin Yang, Vladimir Iglovikov, Anton Dobrenkii, Madhu Reddiboina, Anubhav Reddy, Xingtong Liu, Cong Gao, Mathias Unberath, Myeonghyeon Kim, Chanho Kim, Chaewon Kim, Hyejin Kim, Gyeongmin Lee, Ihsan Ullah, Miguel Luna, Sang Hyun Park, Mahdi Azizian, Danail Stoyanov, Lena Maier-Hein, and Stefanie Speidel. 2018 robotic scene segmentation challenge, 2020. 5, 6, 7, 8, 11, 12, 13
- [3] Max Allan, Jonathan Mcleod, Congcong Wang, Jean Claude Rosenthal, Zhenglei Hu, Niklas Gard, Peter Eisert, Ke Xue Fu, Trevor Zeffiro, Wenyao Xia, Zhanshi Zhu, Huoling Luo, Fucang Jia, Xiran Zhang, Xiaohong Li, Lalith Sharan, Tom Kurmann, Sebastian Schmid, Raphael Sznitman, Dimitris Psychogios, Mahdi Azizian, Danail Stoyanov, Lena Maier-Hein, and Stefanie Speidel. Stereo correspondence and reconstruction of endoscopic data challenge, 2021. 5, 6, 8, 11, 14
- [4] Ang Cao and Justin Johnson. Hexplane: A fast representation for dynamic scenes, 2023. 4, 5, 8
- [5] Cheng Chen, Juzheng Miao, Dufan Wu, Aoxiao Zhong, Zhiling Yan, Sekeun Kim, Jiang Hu, Zhengliang Liu, Lichao Sun, Xiang Li, Tianming Liu, Pheng-Ann Heng, and Quanzheng Li. Ma-sam: Modality-agnostic sam adaptation for 3d medical image segmentation. *Medical Image Analysis*, 98:103310, 2024. 2
- [6] Guikun Chen and Wenguan Wang. A survey on 3d gaussian splatting, 2024. 2
- [7] Jialei Chen, Xin Zhang, Mobarakol Islam, Francisco Vasconcelos, Danail Stoyanov, Daniel S. Elson, and Baoru Huang. Surgicalgs: Dynamic 3d gaussian splatting for accurate robotic-assisted surgical scene reconstruction, 2024. 2
- [8] Long Chen, Wen Tang, Nigel W. John, Tao Ruan Wan, and Jian Jun Zhang. Slam-based dense surface reconstruction in monocular minimally invasive surgery and its application to augmented reality. *Computer Methods and Programs in Biomedicine*, 158:135–146, 2018. 1, 2
- [9] Wei Gao and Russ Tedrake. Surfelwarp: Efficient non-volumetric single view dynamic reconstruction, 2019. 2
- [10] Bernhard Kerbl, Georgios Kopanas, Thomas Leimkühler, and George Drettakis. 3d gaussian splatting for real-time radiance field rendering, 2023. 1, 2, 3, 6
- [11] Diederik P. Kingma and Jimmy Ba. Adam: A method for stochastic optimization, 2017. 5
- [12] Alexander Kirillov, Eric Mintun, Nikhila Ravi, Hanzi Mao, Chloe Rolland, Laura Gustafson, Tete Xiao, Spencer Whitehead, Alexander C. Berg, Wan-Yen Lo, Piotr Dollár, and Ross Girshick. Segment anything, 2023. 2, 4, 11
- [13] Sosuke Kobayashi, Eiichi Matsumoto, and Vincent Sitzmann. Decomposing nerf for editing via feature field distillation, 2022. 2, 9
- [14] Huiqian Li, Dingwen Zhang, Jieru Yao, Longfei Han, Zhongyu Li, and Junwei Han. Asps: Augmented segment anything model for polyp segmentation. In *Medical Image Computing and Computer Assisted Intervention – MICCAI 2024*, pages 118–128, Cham, 2024. Springer Nature Switzerland. 2
- [15] Yang Li, Florian Richter, Jingpei Lu, Emily K. Funk, Ryan K. Orosco, Jianke Zhu, and Michael C. Yip. Super: A surgical perception framework for endoscopic tissue manipulation with surgical robotics. *IEEE Robotics and Automation Letters*, 5(2):2294–2301, 2020. 1, 2
- [16] Zhaoshuo Li, Xingtong Liu, Nathan Drenkow, Andy Ding, Francis X. Creighton, Russell H. Taylor, and Mathias Unberath. Revisiting stereo depth estimation from a sequence-to-sequence perspective with transformers, 2021. 11
- [17] Hengyu Liu, Yifan Liu, Chenxin Li, Wuyang Li, and Yixuan Yuan. Lgs: A light-weight 4d gaussian splatting for efficient surgical scene reconstruction. In *Medical Image Computing and Computer Assisted Intervention – MICCAI 2024*, pages 660–670, Cham, 2024. Springer Nature Switzerland. 1, 5
- [18] Xingtong Liu, Maia Stiber, Jindan Huang, Masaru Ishii, Gregory D. Hager, Russell H. Taylor, and Mathias Unberath. Reconstructing sinus anatomy from endoscopic video – towards a radiation-free approach for quantitative longitudinal assessment, 2020. 1, 2
- [19] Yifan Liu, Chenxin Li, Chen Yang, and Yixuan Yuan. Endogaussian: Real-time gaussian splatting for dynamic endoscopic scene reconstruction, 2024. 1, 2, 3, 4, 5, 6, 7, 8, 13
- [20] Yonghao Long, Zhaoshuo Li, Chi Hang Yee, Chi Fai Ng, Russell H. Taylor, Mathias Unberath, and Qi Dou. E-dssr: Efficient dynamic surgical scene reconstruction with transformer-based stereoscopic depth perception, 2021. 1, 2
- [21] Jingpei Lu, Ambareesh Jayakumari, Florian Richter, Yang Li, and Michael C. Yip. Super deep: A surgical perception framework for robotic tissue manipulation using deep learning for feature extraction, 2021. 2
- [22] Jun Ma, Yuting He, Feifei Li, Lin Han, Chenyu You, and Bo Wang. Segment anything in medical images. *Nature Communications*, 15(1), 2024. 2
- [23] Ricardo Martin-Brualla, Noha Radwan, Mehdi S. M. Sajjadi, Jonathan T. Barron, Alexey Dosovitskiy, and Daniel Duckworth. Nerf in the wild: Neural radiance fields for unconstrained photo collections, 2021. 2
- [24] Ben Mildenhall, Pratul P. Srinivasan, Rodrigo Ortiz-Cayon, Nima Khademi Kalantari, Ravi Ramamoorthi, Ren Ng, and Abhishek Kar. Local light field fusion: Practical view synthesis with prescriptive sampling guidelines, 2019. 11
- [25] Ben Mildenhall, Pratul P. Srinivasan, Matthew Tancik, Jonathan T. Barron, Ravi Ramamoorthi, and Ren Ng. Nerf:

- Representing scenes as neural radiance fields for view synthesis, 2020. 1, 2, 6
- [26] Reda Mithany, Nesma Daniel, Muhammad Shahid, Samana Aslam, Mark Abdelmaseeh, Farid Gerges, Muhammad Gill, Shenouda Abdallah, Abdul Hannan, Muhammad Saeed, Mina Manasseh, and Mohamed Mohamed. Revolutionizing surgical care: The power of enhanced recovery after surgery (eras). *Cureus*, 15, 2023. 1
- [27] Michael Niemeyer and Andreas Geiger. Giraffe: Representing scenes as compositional generative neural feature fields, 2021. 2
- [28] Veronica Penza, Elena De Momi, Nima Enayati, Thibaud Chupin, Jesús Ortiz, and Leonardo S. Mattos. Envisors: Enhanced vision system for robotic surgery. a user-defined safety volume tracking to minimize the risk of intraoperative bleeding. *Frontiers in Robotics and AI*, 4, 2017. 2
- [29] AKM Shahariar Azad Rabby and Chengcui Zhang. Beyond-pixels: A comprehensive review of the evolution of neural radiance fields, 2024. 2
- [30] Nikhila Ravi, Valentin Gabeur, Yuan-Ting Hu, Ronghang Hu, Chaitanya Ryali, Tengyu Ma, Haitham Khedr, Roman Rädle, Chloe Rolland, Laura Gustafson, Eric Mintun, Junting Pan, Kalyan Vasudev Alwala, Nicolas Carion, Chao-Yuan Wu, Ross Girshick, Piotr Dollár, and Christoph Feichtenhofer. Sam 2: Segment anything in images and videos, 2024. 2, 8
- [31] Yawar Siddiqui, Lorenzo Porzi, Samuel Rota Buló, Norman Müller, Matthias Nießner, Angela Dai, and Peter Kotschieder. Panoptic lifting for 3d scene understanding with neural fields, 2022. 2
- [32] Jingwei Song, Jun Wang, Liang Zhao, Shoudong Huang, and Gamini Dissanayake. Dynamic reconstruction of deformable soft-tissue with stereo scope in minimal invasive surgery. *IEEE Robotics and Automation Letters*, 3(1):155–162, 2018. 1, 2
- [33] Aliza Subedi, Smriti Regmi, Nisha Regmi, Bhumi Bhusal, Ulas Bagci, and Debesh Jha. Classification of endoscopy and video capsule images using cnn-transformer model, 2024. 1
- [34] Charlotte Tsui, Rachel Klein, and Matthew Garabrant. Minimally invasive surgery: national trends in adoption and future directions for hospital strategy. *Surgical Endoscopy*, 27(7): 2253–2257, 2013. 1
- [35] Kailing Wang, Chen Yang, Yuehao Wang, Sikuang Li, Yan Wang, Qi Dou, Xiaokang Yang, and Wei Shen. Endogslam: Real-time dense reconstruction and tracking in endoscopic surgeries using gaussian splatting, 2024. 1
- [36] Yuehao Wang, Yonghao Long, Siu Hin Fan, and Qi Dou. Neural rendering for stereo 3d reconstruction of deformable tissues in robotic surgery, 2022. 2, 5, 6, 7, 8, 11, 14
- [37] Zhao Wang, Chang Liu, Shaoting Zhang, and Qi Dou. Foundation model for endoscopy video analysis via large-scale self-supervised pre-train. In *Medical Image Computing and Computer Assisted Intervention – MICCAI 2023*, pages 101–111, Cham, 2023. Springer Nature Switzerland. 2
- [38] Guanjun Wu, Taoran Yi, Jiemin Fang, Lingxi Xie, Xiaopeng Zhang, Wei Wei, Wenyu Liu, Qi Tian, and Xinggang Wang. 4d gaussian splatting for real-time dynamic scene rendering, 2024. 4
- [39] Weixing Xie, Junfeng Yao, Xianpeng Cao, Qiqin Lin, Zerui Tang, Xiao Dong, and Xiaohu Guo. Surgicalgaussian: Deformable 3d gaussians for high-fidelity surgical scene reconstruction, 2024. 2
- [40] Chen Yang, Kailing Wang, Yuehao Wang, Xiaokang Yang, and Wei Shen. Neural lerplane representations for fast 4d reconstruction of deformable tissues, 2023. 2, 4, 5
- [41] Jialin Yu, Huogen Wang, and Ming Chen. Colonoscopy polyp detection with massive endoscopic images, 2022. 1
- [42] Ruyi Zha, Xuelian Cheng, Hongdong Li, Mehrtash Harandi, and Zongyuan Ge. Endosurf: Neural surface reconstruction of deformable tissues with stereo endoscope videos, 2023. 1, 5
- [43] Shuaifeng Zhi, Tristan Laidlow, Stefan Leutenegger, and Andrew J. Davison. In-place scene labelling and understanding with implicit scene representation, 2021. 2
- [44] Haoyin Zhou and Jagadeesan Jayender. Emdq-slam: Real-time high-resolution reconstruction of soft tissue surface from stereo laparoscopy videos. In *Medical Image Computing and Computer Assisted Intervention – MICCAI 2021*, pages 331–340, Cham, 2021. Springer International Publishing. 1, 2
- [45] Haoyin Zhou and Jagadeesan Jayender. Emdq-slam: Real-time high-resolution reconstruction of soft tissue surface from stereo laparoscopy videos. *Medical image computing and computer-assisted intervention : MICCAI ... International Conference on Medical Image Computing and Computer-Assisted Intervention*, 12904:331–340, 2021. 5
- [46] Shijie Zhou, Haoran Chang, Sicheng Jiang, Zhiwen Fan, Zehao Zhu, Dejia Xu, Pradyumna Chari, Suyu You, Zhangyang Wang, and Achuta Kadambi. Feature 3dgs: Supercharging 3d gaussian splatting to enable distilled feature fields, 2024. 2, 4, 8, 9, 11
- [47] Shijie Zhou, Zhiwen Fan, Dejia Xu, Haoran Chang, Pradyumna Chari, Tejas Bharadwaj, Suyu You, Zhangyang Wang, and Achuta Kadambi. Dreamscene360: Unconstrained text-to-3d scene generation with panoramic gaussian splatting. In *Computer Vision – ECCV 2024*, pages 324–342, Cham, 2025. Springer Nature Switzerland. 2
- [48] Jiayuan Zhu, Abdullah Hamdi, Yunli Qi, Yueming Jin, and Junde Wu. Medical sam 2: Segment medical images as video via segment anything model 2, 2024. 1, 2

## A. Appendix A: Dataset Details

This supplementary material provides additional dataset details not included in the main paper.

EndoNeRF [36] comprises two in-vivo prostatectomy cases captured with stereo cameras from a single viewpoint. The dataset features non-rigid deformations and tool occlusions. We also use the Stereo Correspondence and Reconstruction of Endoscopic Data (SCARED) [3] dataset from the 2022 Endoscopic Vision Challenge, which consists of RGB-D scans of porcine cadaver abdominal anatomy collected using a da Vinci Xi endoscope and a projector.

Within the EndoNeRF dataset, the pulling video contains 63 frames. We select every eighth frame for testing, resulting in 58 training frames and 5 test frames. The cutting video comprises 156 frames and is split in a similar manner, yielding 136 training frames and 20 test frames.

For segmentation, we employ the Robotic Scene Segmentation Sub-Challenge from the 2018 Endoscopic Vision Challenge (EndoVis18) [2]. This dataset contains four sequences, each with 149 frames depicting diverse surgical scenes with annotations for various anatomical and tool components. In total, there are ten labels in this multi-label segmentation dataset: background tissue, instrument shaft, instrument clasper, instrument wrist, kidney parenchyma, covered kidney, thread, clamps, suturing needles, suction instrument, and small intestine. The original images are sized at  $1280 \times 1024$  pixels and are downsampled to  $640 \times 512$  pixels for training. Although the original EndoVis18 videos were captured at 60 Hz, they were subsampled to 2 Hz to reduce labeling efforts. Furthermore, sequences with minimal movement were removed, resulting in the final 149-frame video. These postprocessing steps present significant challenges for high-fidelity surgical scene reconstruction. To prepare these images for FEG, we first obtain stereo depth masks using the stereo transformer lite [16]. Additionally, we prepare a camera poses and intrinsics file in the LLFF (Local Light Field Fusion) format [24]. As a simplification, we assume a single viewpoint and set all camera poses to the identity to avoid interference from ill-calibrated poses.

To demonstrate the utility of FEG for segmentation, we select 60 frames from sequence 1, which depict a continuous surgical scene of the kidney. In these frames, a clip applier tool is used, and parts of the small intestine appear in the foreground. These frames were chosen for training because the scene contains multiple key segmentation targets, including the kidney, small intestine, clamps, and all components of grasping instruments (i.e., instrument head, instrument wrist, and instrument clasper). These targets vary in size, segmentation complexity, and instance count per frame, presenting a challenging multilabel segmentation task suitable for evaluating our model. Due to substantial tissue and tool movements and a camera repositioning midway through the scene, we split these 60 frames into two segments for

rendering. The first segment, comprising 33 frames, is processed through our FEG pipeline, while the latter 27 frames are rendered as a separate scene. Aside from the mid-scene movements, the camera remains fairly stable, with smooth transitions and consistent overlap in scene coverage, ensuring a well-constrained reconstruction. During segmentation, we aggregate the feature maps from these two segments to benchmark against standalone SAM models.

## B. Appendix B: Additional Details of Integrating Semantic Features into FEG

This supplementary material provides additional details on integrating semantic features into FEG that were not included in the main paper.

For segmentation experiments, we use SAM’s pretrained ViT-H encoder to generate a ground truth feature map for each frame in our video snippet. As detailed in SAM [12], the image encoder is pretrained via MAE and employs  $14 \times 14$  windowed attention along with four equally spaced global attention blocks. The resulting feature maps have dimensions of  $256 \times 64 \times 64$ , which are then resized to  $256 \times 51 \times 64$  to match the aspect ratio of the training image. This resizing is accomplished by simply cropping the feature map height, as done in Feature 3DGS [46]. Since only a portion of the  $64 \times 64$  feature map contains semantic information due to padding, we crop the side corresponding to the longer dimension of the original image.

For segmentation, we use the same configuration as with the EndoNeRF cutting dataset. We note that no hyperparameter tuning has been performed for the EndoVis dataset, and performance metrics may be further improved with additional tuning. After running FEG, the generated feature maps are directly fed into the pretrained SAM decoder to produce multilabel segmentations. Prior to this step, all feature maps are restored to their original aspect ratio of  $64 \times 64$  via bilinear interpolation. For the segmentation prompt, bounding boxes computed from the ground truth mask for each class are used. If a class appears in multiple masks within an image, bounding boxes are computed for each instance.

## C. Appendix C: Finetuning SAM Details

We use the SAM model with the ViT-B encoder and standard pretrained weights. Instead of fully finetuning all layers, we adopt the “adapter” training strategy proposed by Gu et al., finetuning only the adapter layer parameters while keeping the rest of the SAM backbone frozen. This significantly reduces VRAM consumption during training, allowing us to work within our limited computational resources. For training, we use sequences two, three, and four from EndoVis18, each containing 149 frames, for a total of 447 images. Sequence one, which also contains 149 images, is reserved for validation and is excluded from training because it is later

used for zero-shot segmentation in Tables 4 and 5.

The preprocessing steps are straightforward: images are normalized and resized. The loss function is defined as the sum of Dice Loss and Cross Entropy. We employ an Adam optimizer with a base learning rate of  $1 \times 10^{-3}$  and a StepLR scheduler with a step size of 10 and  $\gamma = 0.5$ . The batch size is set to 4, and validation is performed every other epoch. Hyperparameters are not tuned; training continues until the validation loss does not decrease for more than 20 epochs. In total, we train for 66 epochs, achieving the best validation score of 0.955 at epoch 46.

Subsequently, we extract embeddings from this finetuned model to serve as the ground truth feature embeddings for our FEG pipeline. Zero-shot segmentation is performed using the semantic feature maps generated by FEG on 60 selected image frames from EndoVis18 for binary segmentation. For this experiment, we follow the same 7:1 train-test split as in EndoNeRF, which enables us to obtain performance metrics on the test set. Segmentation performance is measured via micro-averaging across all classes on the train image frames, with each label weighted by its mask size, and we observe a marked improvement when using these finetuned features compared to the baseline.

## D. Appendix D: Additional Visualizations

### D.1. Additional Segmentation Visualizations

We provide additional visualizations of the rendered, decoded semantic features of FEG and compare them with the zero-shot segmentations from 2D foundation models in Figure 4.

### D.2. Additional Rendering Visualizations

We provide additional visualizations of rendering on the EndoVis18 dataset [2] in Figure 5.

## E. Rasterizer

Our rasterizer incorporates several enhancements to effectively render color, depth, and semantic feature maps concurrently. It works by rasterizing Gaussian primitives into image space while maintaining differentiability, thereby enabling gradient propagation back to each Gaussian’s parameters. During the backward pass, gradients are accumulated for each Gaussian primitive—encompassing color, depth, opacity, semantic features, and covariance matrices. Enhanced alpha blending techniques ensure numerical stability and smoother gradient flows for transparent Gaussians, which significantly reduces the rendering artifacts observed in earlier versions of the rasterizers.

## F. Training hyperparameters

In Table 8, we present the hyperparameter configurations used in our experiments for the EndoNeRF and SCARED

datasets. Most other hyperparameters remain fixed at the default values provided in the code.

We observed stability issues during the fine stage on the EndoNeRF dataset, likely due to our model’s enhanced rendering performance during the coarse stage, which is attributed to our revamped rasterizer. An excessively high PSNR during the coarse phase—reaching up to 50—indicated overfitting during initialization with a single image, thereby hindering subsequent deformation optimization. Although the first 100–300 iterations of the fine stage showed promising convergence, the model occasionally experienced an abrupt drop in PSNR, sometimes as low as 5. To maintain stable training dynamics and ensure generalizable deformation capabilities, it was necessary to adjust hyperparameters, particularly by reducing the learning rates and fine-tuning gradient propagation strategies. Furthermore, the coarse initialization stage must be capped to conclude at a lower PSNR to ensure stability during the fine deformation stage.



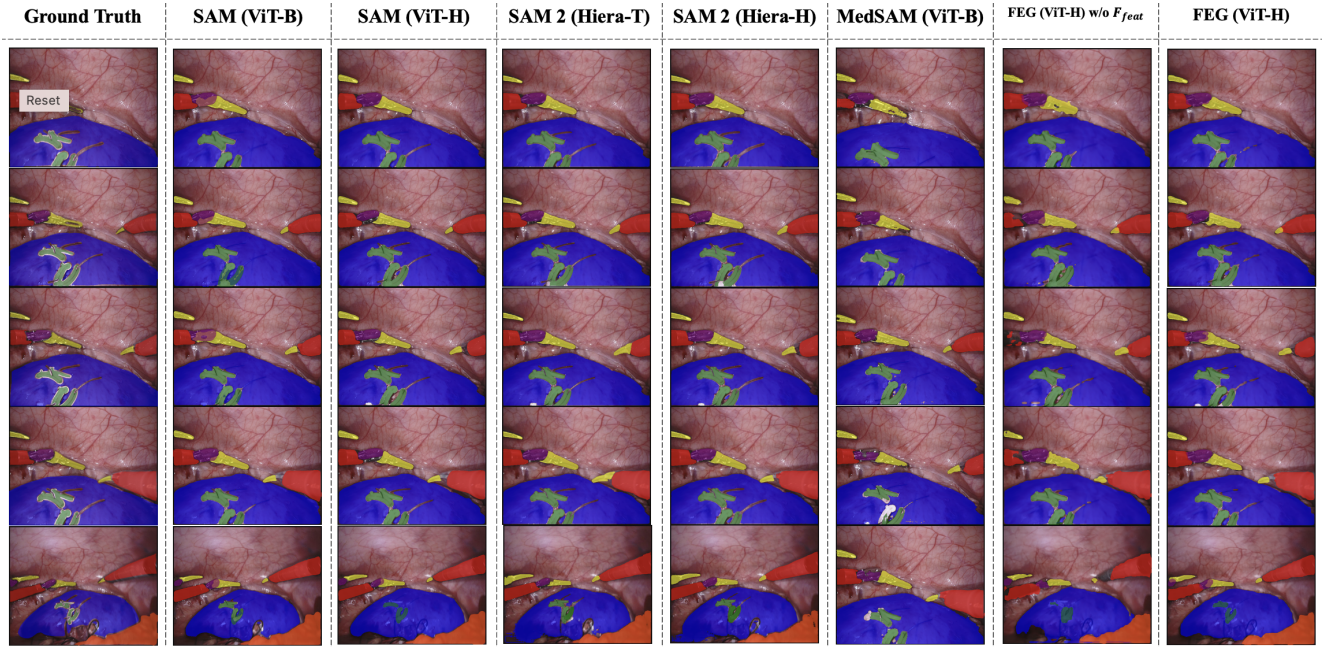


Figure 4. Additional qualitative segmentation comparisons. From left to right: our full FEG model, FEG without the 5th MLP, MedSAM (ViT-B), SAM 2 (Hiera-H), SAM 2 (Hiera-T), SAM (ViT-H), SAM (ViT-B), and the ground truth segmentation mask. Colors correspond to the following classes: kidney (blue), small intestine (orange), instrument shaft (red), instrument clasper (yellow), instrument wrist (purple), and clamps (green).

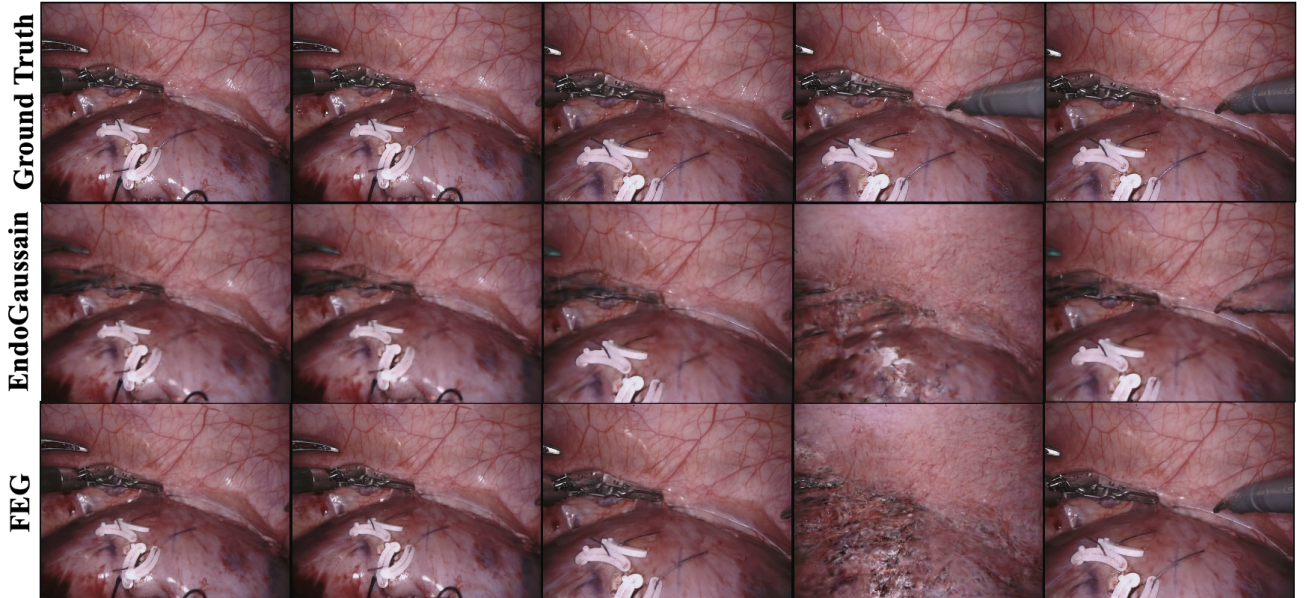


Figure 5. Comparison of qualitative renderings between EndoGaussian [19], FEG, and ground truth on the EndoVis18 dataset [2]. We can see that across all scenes, FEG and EndoGaussian experience similar performances, although FEG is able to capture semantic features which can then later be used for segmentation.

Table 8. Hyperparameter Settings for pulling and cutting sets from EndoNeRF [36] and the SCARED dataset [3].

<b>Hyperparameter</b>	<b>EndoNeRF Pulling</b>	<b>EndoNeRF Cutting</b>	<b>SCARED</b>
Initial Points	90,000	90,000	30,000
Grid LR (Initial / Final)	0.0032 / 0.0000032	0.0016 / 0.0000016	0.0016 / 0.000016
Deformation LR (Initial / Final)	0.00016 / 1.6e-7	0.0004 / 4e-7	0.00008 / 0.0000008
Position LR (Initial / Final)	0.00016	0.00016	0.00016 / 0.0000016
Iterations (Coarse / Fine)	1000 / 6000	1000 / 6000	1000 / 3000
Percent Dense	0.01	0.01	0.01
Opacity Reset Interval	6000	6000	3000
Prune Interval	6000	6000	3000
Position LR Max Steps	7000	7000	3000
Deformation LR Delay Multiplier	0.01	0.01	0.01
Grid Dimensions	2	2	2
Input Coordinate Dim	4	4	4
Output Coordinate Dim	64	64	32
Multiresolution Levels	[1,2,4,8]	[1, 2, 4, 8]	[1, 2, 4, 8]